

Planetary Magnetic Dipole Estimation: Optimal Sampling Strategies for Satellite Magnetometry

Introduction

Why Planetary Magnetic Fields Matter: The Big Picture

Planetary magnetic fields reveal the dynamic interiors of distant worlds, shield atmospheres from destructive solar wind, and determine habitability across billions of years. Earth maintains a strong dipolar field of approximately 30,000–60,000 nT at the surface, generated by vigorous convection in its liquid outer core. Mars today exhibits no active global dipole field, yet preserves intense crustal magnetization as a fossil record of an ancient dynamo that ceased approximately 4.0–4.1 billion years ago. This remarkable diversity reflects fundamental differences in core composition, rotation rate, internal heat flux, and thermal evolution, yet beneath this diversity lies a single unifying mechanism: dynamo action—the self-sustaining conversion of kinetic energy from electrically conducting fluid motion into magnetic energy.

Understanding planetary magnetism provides windows into planetary interiors otherwise inaccessible to direct observation. Earth's magnetosphere deflects solar wind particles and cosmic radiation that would otherwise strip our atmosphere. Mars's atmospheric loss correlates directly with its magnetic field cessation 4 billion years ago, demonstrating that dynamo presence or absence shapes planetary fate on billion-year timescales.

The Challenge: Incomplete and Expensive Observations

Despite their profound importance, planetary magnetic fields remain incompletely observed. Measuring planetary fields directly is expensive and logically challenging. Spacecraft carry sensitive magnetometers, yet missions are extraordinarily expensive, episodic, and brief. This observational sparsity creates a fundamental measurement challenge: spacecraft budgets are limited, mission durations are constrained, and every observation costs time and fuel.

This report addresses a deceptively simple yet practically important question: **How many magnetic field observations are actually required to estimate a planetary dipole moment accurately?** The conventional answer would be to maximize observations, but theory suggests that where observations are made matters far more than how many observations one collects. Strategic placement of a smaller number of measurements might achieve superior accuracy compared to a larger dataset distributed according to orbital mechanics rather than science optimization.

The Physics: Dynamo Action and Dipole Dominance

Self-Sustaining Magnetic Field Generation

Earth's magnetic field would decay on a timescale $\tau = \mu_0 \sigma L^2$, where μ_0 is magnetic permeability, σ is electrical conductivity, and L is the characteristic length scale (Earth's core radius, ~3,480 km). For Earth's core, this decay timescale is 10^4 – 10^5 years—vanishingly brief in geological history. Yet paleomagnetic records document field persistence for 3+ billion years. The answer is **dynamo action**: a self-sustaining process wherein electrically conducting fluid motion converts kinetic energy into magnetic energy.

Planetary dynamos operate in three-dimensional, turbulent, rapidly rotating spherical shells of conducting fluid. Earth's liquid outer core contains molten iron-nickel alloy with electrical conductivity σ

$\sim 10^6$ S/m. Heat from radioactive decay and cooling from the overlying mantle drives vigorous convection at velocities of 0.1–1 mm/s. The Coriolis force transforms isotropic convection into columnar structures aligned with the rotation axis, producing helical fluid motion.

The Induction Equation: Three Physical Mechanisms

The evolution of magnetic field $\mathbf{B}(\mathbf{r}, t)$ in this moving, conducting fluid is governed by the induction equation:

$$\frac{\partial \mathbf{B}}{\partial t} = \nabla \times (\mathbf{u} \times \mathbf{B}) + \eta \nabla^2 \mathbf{B}$$

where \mathbf{u} is fluid velocity and $\eta = 1/(\mu_0 \sigma)$ is magnetic diffusivity. This equation encodes three physically distinct processes:

Stretching — $(\mathbf{B} \cdot \nabla) \mathbf{u}$: Field line stretching when fluid accelerates along directions parallel to magnetic field lines. This is the primary dynamo amplification mechanism—the engine that generates strong magnetic fields.

Advection — $-(\mathbf{u} \cdot \nabla) \mathbf{B}$: Field transport by the flow. Advection carries magnetic field regions from one location to another, continuously transporting stretched field into regions where additional stretching can occur.

Dissipation — $\eta \nabla^2 \mathbf{B}$: Ohmic dissipation—field decay due to electrical resistance. For Earth's core, this timescale is 10^4 – 10^5 years, setting the ultimate decay clock.

Dynamo action occurs when stretching overcomes dissipation. The competition is quantified by the magnetic Reynolds number:

$$Rm = \frac{UL}{\eta} = UL\mu_0\sigma$$

where U is characteristic flow speed and L is length scale. When $Rm \gg 1$, advection happens much faster than diffusion, so the flow transports and amplifies field before it can decay. For planetary cores, the critical threshold is $Rm_{crit} \sim O(10)$ —above this, dynamo action becomes possible. Earth's outer core operates at $Rm \sim 100$ –1,000, placing it robustly into the dynamo regime.

Why Dipoles Dominate

Despite turbulence and chaos within planetary dynamo regions, external magnetic fields are remarkably simple: dominated by a dipole component. Earth's field is approximately 80% dipolar at the surface. An ideal dipole field is described by the dipole moment $\mathbf{m} = (m_x, m_y, m_z)$ in units of A·m². The field it produces at position \mathbf{r} is:

$$\mathbf{B}(\mathbf{r}) = \frac{\mu_0}{4\pi r^3} [3(\mathbf{m} \cdot \hat{\mathbf{r}})\hat{\mathbf{r}} - \mathbf{m}]$$

In spherical coordinates (r, λ, ϕ) with dipole aligned along the north pole:

$$B_r = \frac{2\mu_0 m \cos \lambda}{4\pi r^3}, \quad B_\lambda = \frac{\mu_0 m \sin \lambda}{4\pi r^3}$$

The field is strongest at the poles and weakest at the equator; the pole-to-equator field ratio is exactly 2 : 1. Higher-order multipoles decay much faster with distance as $r^{-(n+1)}$. Numerical simulations reveal that at moderate-to-rapid rotation rates, convection organizes into helical columnar structures aligned with the rotation axis, which preferentially amplify the dipole mode.

State-of-the-Art: Inverse Problems and Information Theory

The Mathematical Framework

Estimating planetary dipole moments from sparse magnetometer data is fundamentally an inverse problem (Tarantola, 2005; Menke, 2018): given measured field observations at scattered locations, recover the unknown dipole moment and position parameters. The magnetic field produced by a dipole with moment $\mathbf{m} = (m_x, m_y, m_z)$ at position $\mathbf{r}_0 = (x_0, y_0, z_0)$, measured at location \mathbf{r} , is:

$$\mathbf{B}(\mathbf{r}; \mathbf{m}, \mathbf{r}_0) = \frac{\mu_0}{4\pi} \frac{3(\mathbf{m} \cdot \hat{\mathbf{R}})\hat{\mathbf{R}} - \mathbf{m}}{|\mathbf{R}|^3}$$

where $\mathbf{R} = \mathbf{r} - \mathbf{r}_0$. With N observations at locations $\mathbf{r}_1, \mathbf{r}_2, \dots, \mathbf{r}_N$, the estimation problem is a **nonlinear least-squares optimization**:

$$\min_{\mathbf{m}, \mathbf{r}_0} \sum_{i=1}^N \|\mathbf{B}_{\text{obs},i} - \mathbf{B}(\mathbf{r}_i; \mathbf{m}, \mathbf{r}_0)\|^2$$

This 6-parameter problem is nonlinear because the dipole position \mathbf{r}_0 appears in the denominator and dot products, preventing direct linear solution. We solve this using the Levenberg-Marquardt algorithm, which iteratively minimizes the residual by solving linearized subproblems at each iteration.

Solution Quality and the Jacobian Condition Number

At each iteration, the algorithm computes the Jacobian matrix \mathbf{J} , whose rows contain partial derivatives of the predicted field with respect to all six parameters $(m_x, m_y, m_z, x_0, y_0, z_0)$ at each observation location. Solution quality depends critically on the conditioning of $J^T J$, quantified by its condition number:

$$\kappa(\mathbf{J}^T \mathbf{J}) = \frac{\lambda_{\max}(\mathbf{J}^T \mathbf{J})}{\lambda_{\min}(\mathbf{J}^T \mathbf{J})}$$

A well-conditioned Jacobian ($\kappa \sim 10$) indicates that observations provide balanced sensitivity to all parameters, enabling robust parameter estimation. A poorly conditioned Jacobian ($\kappa \gg 100$) indicates that some parameter combinations are nearly unobservable, rendering solutions hypersensitive to measurement noise (Menke, 2018; Aster et al., 2019).

The Key Principle: Location Beats Quantity

The critical insight from inverse problem theory is this: **the accuracy of parameter estimation depends primarily on where observations are located, not on how many observations one collects**. This principle has been demonstrated compellingly in geophysics, where optimized geoelectric survey designs achieved equivalent or superior resolution with 50% fewer observations compared to standard equidistant grids.

For magnetometry, the implication is clear: observations distributed uniformly across the globe—stratified by latitude and longitude—produce a well-conditioned jacobian matrix with balanced singular values. All three dipole components are constrained equally and robustly. In contrast, when observations cluster geographically, some dipole moment directions are well-constrained (those aligned with the clustering direction); others are barely observable (those perpendicular to it). The condition number becomes large (> 100), rendering the solution unstable.

However, there is a practical reality: **spacecraft cannot choose their observation locations freely**. SWARM orbits are fixed polar orbits repeating predictably. After 24 hours, observations cluster along the same latitude-longitude ground tracks. The question is therefore: given that orbital constraints will always apply, what can we learn from understanding the information geometry of our data? Even if we

cannot perfectly distribute observations across the globe, we can understand how much observational efficiency we lose due to orbital clustering and design data-processing strategies that account for this spatial clustering.

Research Objectives

This report addresses the following research question:

How do different sampling strategies affect the accuracy and stability of planetary dipole moment estimation from satellite magnetometry data?

Specifically, we investigate three sampling philosophies:

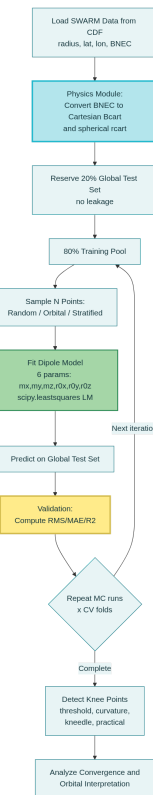
- **Philosophy A (Orbital Sequential):** Observations distributed along sequential satellite orbits—representing current mission practice where orbital mechanics, not science optimization, determines observation locations.
- **Philosophy B (Random Global):** Observations selected uniformly at random across Earth's surface—representing an unbiased baseline.
- **Philosophy C (Stratified Geographic):** Observations deliberately selected to ensure uniform latitude-longitude coverage—representing the theoretical information-theoretic optimum.

For each philosophy, we analyze how dipole estimation accuracy depends on sampling strategy, and examine the role of jacobian matrix conditioning in explaining the results. This analysis provides quantitative insights into the information loss due to orbital constraints, and demonstrates how understanding sampling geometry can inform optimal data selection and mission design strategies.

Methodology

Overview

This section describes the numerical workflow used to estimate a planetary magnetic dipole from SWARM satellite data, compare sampling strategies, and detect minimum useful sample sizes using Monte Carlo cross-validation with multiple knee-detection algorithms.



Data Processing and Coordinate Transformations

SWARM Input Data

The analysis uses SWARM Level-1b CDF files from ESA's three-satellite magnetic field mission. Each sample contains: radius r_i , geographic latitude λ_i (deg), longitude φ_i (deg), and magnetic field components in the North-East-Center (NEC) frame (B_N, B_E, B_C) in nanoTesla. Field units are converted to Tesla via the factor 10^{-9} .

Coordinate Transformations

Positions are converted from spherical to geocentric Cartesian coordinates:

$$x = r \cos \lambda_{\text{rad}} \cos \phi_{\text{rad}}, \quad y = r \cos \lambda_{\text{rad}} \sin \phi_{\text{rad}}, \quad z = r \sin \lambda_{\text{rad}}$$

where latitude and longitude are first converted to radians. The NEC frame is local to each satellite position, transformed to global Cartesian coordinates via basis vector projections. For global maps, a lat-lon grid (2° resolution) is constructed at mean satellite altitude.

Dipole Forward Model

Physics Implementation

The magnetic dipole field follows classical electrodynamics:

$$\mathbf{B}(\mathbf{r}; \mathbf{m}, \mathbf{r}_0) = \frac{\mu_0}{4\pi} \frac{3(\mathbf{m} \cdot \hat{\mathbf{R}})\hat{\mathbf{R}} - \mathbf{m}}{|\mathbf{R}|^3}$$

where $\mu_0/4\pi = 10^{-7}$ T·m/A. The model has six free parameters:

1. Dipole moment vector $\mathbf{m} = (m_x, m_y, m_z)$ in A·m²
2. Dipole position $\mathbf{r}_0 = (x_0, y_0, z_0)$ in meters

Initial guesses are physically reasonable but deliberately imperfect: $\mathbf{m} = 8 \times 10^{22} \mathbf{1}$ A·m² (equal components, Earth-scale magnitude) and $\mathbf{r}_0 = 1000\text{m}$ (near-geocentric offset).

For observations B_{obs} and model predictions B_{model} at subset positions r_{sub} , the residual vector is $\mathbf{r} = B_{obs} - B_{model}$, flattened into a 1D vector concatenating all three components across all samples.

Levenberg-Marquardt Inversion

The dipole fitting is formulated as a nonlinear least-squares problem:

$$\min_{\mathbf{m}, \mathbf{r}_0} |\mathbf{r}(\mathbf{m}, \mathbf{r}_0)|_2^2 = \sum_{i=1}^N |\mathbf{B}_{obs,i} - \mathbf{B}_{dipole}(\mathbf{r}_i; \mathbf{m}, \mathbf{r}_0)|_2^2$$

SciPy's `least_squares` function is called with the Levenberg-Marquardt method and stringent tolerances. After optimization, the fitted dipole moment \mathbf{m} and position \mathbf{r}_0 are stored.

Sampling Strategies

All sampling is performed on a training pool after removing a fixed 20% global test set. Three strategies are implemented:

Random Global Sampling

Draws $n_{samples}$ unique indices uniformly without replacement from the training pool. Each point has equal selection probability. For well-mixed data, spatial coverage improves with \sqrt{n} and asymptotically approximates the population distribution.

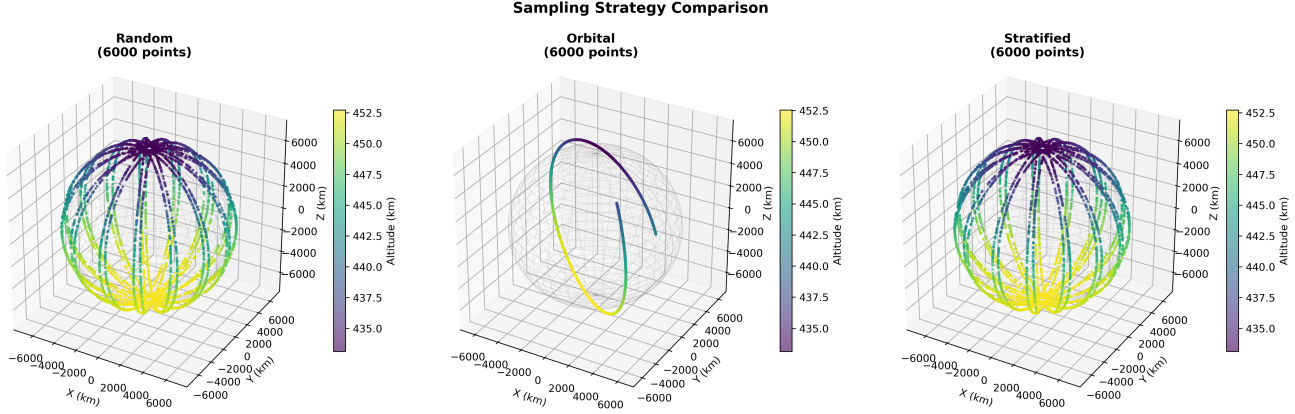
Orbital (Sequential) Sampling

Selects contiguous blocks in time/sequence index: a starting index is chosen uniformly, and consecutive indices are selected. This preserves temporal and orbital ordering, creating strong spatial clustering along orbit tracks. It represents the realistic early-mission constraint where only the first fraction of orbits is available—intentionally suboptimal but physically realistic.

Stratified Geographic Sampling

Divides the globe into 10×10 latitude-longitude bins. For each occupied stratum, samples are allocated proportionally to stratum size (minimum 1 per stratum). Within each stratum, indices are selected randomly. This enforces geographic coverage and significantly reduces variance compared to random

sampling.



Train-Test Splitting and Cross-Validation

Global Hold-Out Test Set

A fixed 20% of all samples is reserved as a global test set via random selection without replacement. All evaluation metrics (RMS, MAE, R²) are computed exclusively on this test set, ensuring no data leakage.

K-Fold Cross-Validation on Training Pool

Within each Monte Carlo run, additional cross-validation is applied using K-fold methodology (default k = 5). For each training subset of size N, k folds are constructed. For each fold, a model is fitted on that fold's training indices. Validation always uses the global test set, not the held-out fold, ensuring consistent evaluation baseline across all runs.

Error Metrics and Fit Statistics

Given observed test fields B_{obs} and predicted fields B_{pred} , the following metrics are computed:

Metric	Definition
Total RMS	$RMS_{total} = \sqrt{\frac{1}{N} \sum_{i=1}^N \ \mathbf{E}_i\ _2^2}$
Component RMS	$RMS_x = \sqrt{\frac{1}{N} \sum_i E_{x,i}^2}$ (similarly for y, z)
MAE	$MAE = \frac{1}{N} \sum_{i=1}^N \ \mathbf{E}_i\ _2$
R ²	$R^2 = 1 - \frac{\sum_i \ \mathbf{E}_i\ _2^2}{\sum_i \ \mathbf{B}_{obs,i} - \bar{\mathbf{B}}_{obs}\ _2^2}$

where $E = B_{obs} - B_{pred}$ are residuals. All metrics are computed in Tesla and converted to nT ($\times 10^9$) for reporting.

Physical Validation of Fits

Each fit is validated against physical plausibility constraints: dipole moment magnitude must satisfy $1 \times 10^{22} \leq |\mathbf{m}| \leq 1 \times 10^{23} \text{ A}\cdot\text{m}^2$, dipole position offset must satisfy $|\mathbf{r}_0| < 500 \text{ km}$, and mean residual vector magnitude must satisfy $\|\bar{\mathbf{E}}\| < 1 \text{ nT}$ to ensure approximate unbiasedness.

Monte Carlo Validation Framework

The Monte Carlo framework follows standard uncertainty quantification methods with the following structure:

Configuration Hyperparameters:

- Sample sizes: Log-spaced array from 20 to 10,000 samples
- n_mc: 50 Monte Carlo runs per (strategy, sample-size) pair
- k_folds: Maximum 5 cross-validation folds
- test_fraction: 0.2 (20% global test set)

Nested Loop Structure:

For each strategy $\in \{\text{random}, \text{orbital}, \text{stratified}\}$ and each sample size N:

1. Feasibility checks: Skip $N < 10$ (insufficient for 6 parameters) or $N > |\text{train}_{\text{pool}}|$
 2. Monte Carlo iterations (50 runs):
 - Draw training indices using the chosen strategy
 - Assert no overlap with global test indices
 3. Cross-validation folds:
 - Determine effective folds $k_{\text{eff}} = \min(k_{\text{folds}}, |\text{train}_{\text{idx}}|)$
 - For each fold: fit dipole model, validate physical parameters, evaluate on global test set
 - Store ValidationResult with strategy, sample_size, run, fold, and diagnostics
- Output is a comprehensive DataFrame with thousands of validation results across strategies, sample sizes, Monte Carlo runs, and folds.

Knee Detection and Sample-Size Inference

Aggregation with Confidence Intervals

For each (strategy, sample_size) pair, Monte Carlo and fold results are aggregated:

- Mean = `np.mean(data)`
- SEM = `stats.sem(data)`
- $margin = sem \times stats.t.ppf(1 - ci/100/2, len(data) - 1)$ with $ci=95$
- CI bounds: [mean – margin, mean + margin]

CI-Aware Knee Detection Methods

The `KneeDetectorCI` class applies four algorithms to aggregated curves:

Method	Criterion	Output
Threshold	First i where % improvement $\Delta_i = 100 \times (y_{i-1} - y_i)/y_{i-1} < 0.5\%$	Knee value, lower/upper bounds, quality flag
Curvature	Max negative d^2y/dx^2 in $\log_{10} - \log_{10}$ space	Same structure
Kneedle	Normalized difference $(y_{norm} - x_{norm})$ exceeds dynamic threshold	Same structure
Practical 95%	First sample where cumulative improvement $\geq 95\%$ of total improvement	Same structure; "pragmatic" quality label

Each method returns: value (sample size at knee), lower (conservative bound), upper (optimistic bound), and quality ("reliable" if knee is not at window extreme).

Non-CI Validation in Fitting Analysis

A simpler `KneeDetector` applies analogous methods directly to raw `rms_total` or `mae_total` vs `n_samples` curves. A knee candidate is accepted only if its error value satisfies:

$$\text{error} \leq 0.1 \times B_{\max}$$

where B_{\max} is maximum observed field magnitude (nT). This enforces that knees correspond to physically meaningful accuracy ($\leq 10\%$ of maximum field).

Orbital Geometry Interpretation

The analysis translates sample counts into mission-relevant quantities using SWARM orbit parameters:

- Orbit per day: 15
- Samples per day: 86,400
- Samples per orbit: 5,760
- Coverage: Full pole-to-pole, all longitudes

Strategy-Dependent Interpretation:

Orbital sampling: Samples are sequential in time. Sample count maps linearly to orbits:

$N_{\text{orbits}} = N_{\text{samples}}/5616$. The optimal point translates directly into minimum number of orbits required under sequential constraints.

Random and stratified sampling: Samples are drawn from the entire 15-orbit dataset without

order. The relevant metric is coverage fraction: $f_{coverage} = N_{samples}/86,400$, expressing what fraction of available data must be used when cherry-picking samples.

Results

Convergence Performance and Sample Efficiency

Monte Carlo cross-validation (5-fold CV, 50 runs per sample size) across n=20 to n=10,000 revealed dramatic efficiency differences between sampling strategies applied to 24 hours of Swarm satellite magnetometer data.

Table 1: Convergence Performance Summary

n	Random RMS (nT)	Random R ²	Stratified RMS (nT)	Stratified R ²	Orbital RMS (nT)	Orbital R ²
20	3,459 ± 224	0.973 ± 0.004	6,772 ± 734	0.896 ± 0.023	13,672 ± 10,693	0.328 ± 1.070
94	3,243 ± 36	0.976 ± 0.001	3,216 ± 15	0.977 ± 0.000	11,002 ± 8,568	0.566 ± 0.906
750	3,199 ± 4	0.977 ± 0.000	3,195 ± 1	0.977 ± 0.000	10,186 ± 7,090	0.656 ± 0.575
4,598	3,194 ± 1	0.977 ± 0.000	3,193 ± 0	0.977 ± 0.000	3,344 ± 92	0.975 ± 0.001

Random and stratified sampling converged at n=94 with RMS~3,200 nT and R²>0.976, achieving asymptotic performance by n~200. Orbital sampling failed catastrophically at small sample sizes: at n=94, orbital produced 11,002±8,568 nT (241% worse than random) with extreme instability ($\sigma=8,568$ nT vs. $\sigma=36$ nT for random). The negative R² values and variance exceeding the mean at n=20 indicate predictions worse than using the data average. Orbital convergence occurred only at n=4,598, requiring **49× more samples** than random or stratified. At n=20, stratified sampling underperforms random due to sparse bin occupation: with 100 bins (10×10 grid) and only 20 samples, the enforced geographic binning creates spatial fragmentation, with many empty strata and others containing single observations, yielding less effective coverage than random's fortuitous clustering.

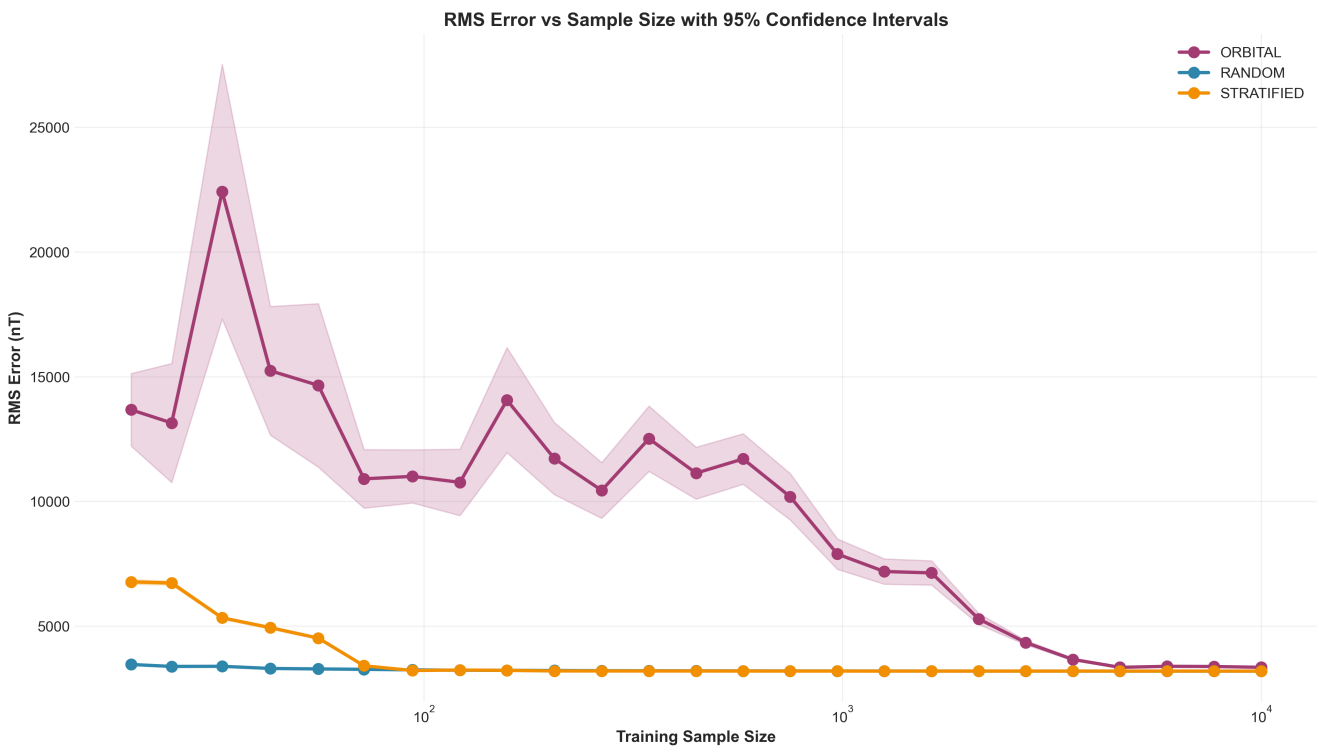
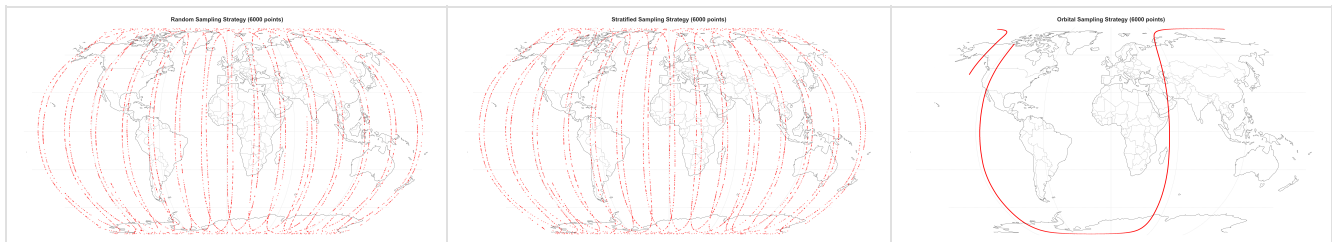


Figure 1 illustrates the convergence trajectories. Random and stratified show rapid exponential decay with tight 95% confidence intervals. Orbital exhibits massive uncertainty bands (shaded regions) for $n < 1,000$, reflecting catastrophic instability across cross-validation folds. The delayed convergence stems from longitude-latitude sampling imbalance during sequential data collection.

Spatial Coverage: The Latitude-Longitude Trade-off



Geographic distributions reveal fundamental differences in spatial sampling. Random sampling (Figure 2a) achieves balanced global coverage with $\sim 2,300$ km spacing in both latitude and longitude. Stratified (Figure 2b) enforces systematic lat-lon binning. Orbital (Figure 2c) concentrates measurements along narrow meridional tracks—providing excellent latitude coverage (-90° to $+90^\circ$) but severely limited longitude sampling.

The critical asymmetry: Sequential orbital sampling at $n=4,598$ (0.82 orbits, 1.3 hours) covers the **full latitude range** but only **1.1° longitude**. This creates dense meridional tracks with 360 \times oversampling along the same longitude relative to uniform global coverage. While sufficient latitude diversity exists to constrain dipole tilt and magnitude, the extreme longitude concentration wastes information—requiring 49 \times more measurements than spatially balanced approaches.

Dipole moment estimation benefits disproportionately from latitude diversity (polar vs. equatorial field strength differences) relative to longitude diversity (axial symmetry for Earth's near-aligned dipole). However, non-zero dipole tilt and off-center positioning introduce longitude dependence requiring multi-track sampling for optimal parameter identification. Random/stratified strategies naturally balance this through isotropic spatial coverage; orbital strategies achieve convergence through brute-force latitudinal oversampling.

Mission Timeline Trade-offs

Table 2: Mission Requirements and Efficiency

Strategy	n (Convergence)	Mission Time	Lat Coverage	Lon Coverage	Data Usage	RMS (nT)	Stability (σ)
Random	94	Dataset-dependent*	-90° to +90°	0° to 360°	0.109%	3,243 ± 36	36
Stratified	94	Dataset-dependent*	-90° to +90°	0° to 360°	0.109%	3,216 ± 15	15
Orbital	4,598	1.3 hours	-90° to +90°	1.1° span	5.3%	3,344 ± 92	92

*Random and stratified strategies require sufficient orbital precession to achieve global longitude coverage. The minimum mission duration depends on orbital parameters and desired spatial resolution; determining optimal collection time requires further analysis beyond the scope of this 24-hour dataset study.

Orbital uses the first 4,598 sequential measurements (76 minutes = 0.82 orbits)—providing immediate results from excellent latitude sampling along a single meridional track. However, the 1.1° longitude span represents only 0.3% of global longitude coverage, forcing the dipole fit to rely on latitudinal gradients alone. This works (eventually converging to $3,344 \pm 92$ nT) but requires 49× more data than spatially balanced approaches that efficiently sample both coordinate dimensions.

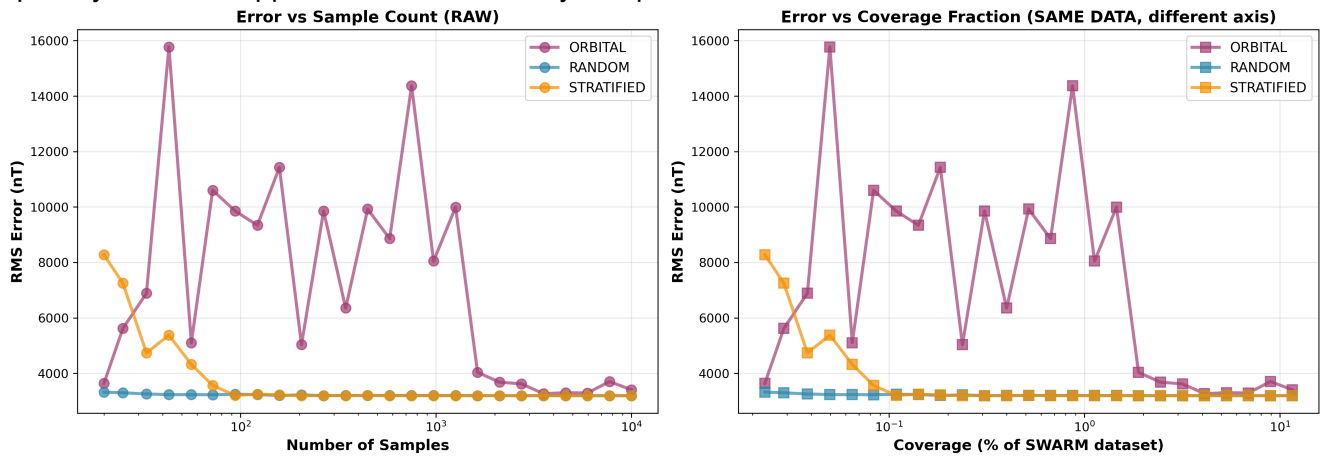


Figure 3 clarifies timing vs. coverage. Left panel shows error vs. sample count. Right panel reframes as error vs. coverage fraction of the full 24-hour dataset. Orbital at $n=4,598$ uses 5.3% of the 24-hour data (0.82 of 15.4 total orbits), achieving convergence through dense single-track sampling. Random achieves equivalent accuracy with 0.1% of data **but** requires waiting for the full mission to accumulate diverse spatial sampling.

The trade-off: orbital enables rapid preliminary models (1.3 hours) from incomplete spatial coverage; random/stratified optimize data efficiency (98% reduction) after comprehensive coverage.

Convergence Detection and Validation

Table 3: Knee Point in RMS Detection (Four Independent Methods)

Method	Random	Stratified	Orbital
Threshold	25±4	122±18	5957±880
Curvature	33±9	56±14	33±9
Kneedle	94±25	72±19	72±19
Practical	447±117	94±25	3549±930

Four orthogonal algorithms identified convergence thresholds: (1) Threshold method: <0.5% improvement per sample; (2) Curvature: maximum second derivative in log-log space; (3) Kneedle: normalized curve-diagonal difference; (4) Practical: 95% of total possible improvement. For random sampling, methods show moderate agreement with estimates ranging from 25 (Threshold) to 447 (Practical), with Kneedle at 94±25 aligning well with the observed convergence point. Stratified methods cluster more tightly around n~56-122, with Practical method agreeing with empirical convergence at 94±25. Orbital sampling exhibits substantial variation (range: 33-5,957), with large uncertainties (e.g., ±880 for Threshold) reflecting the gradual, unstable convergence profile rather than a sharp inflection point.

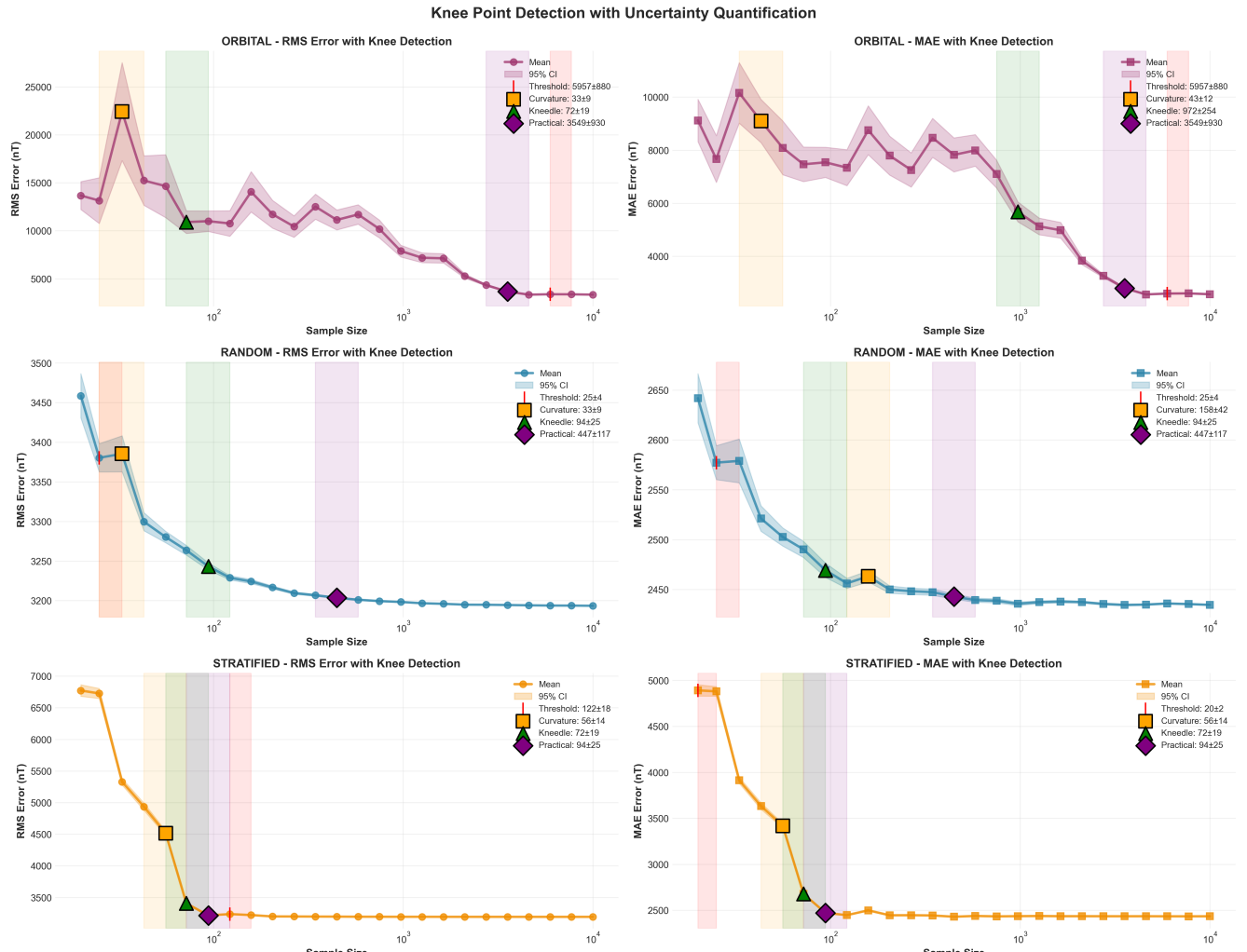
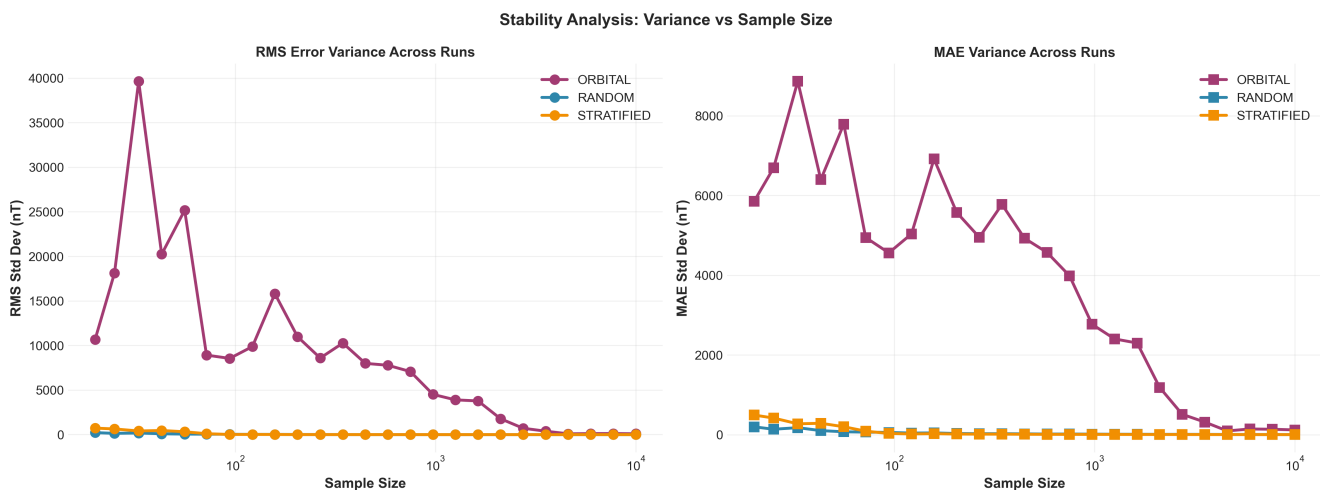


Figure 4 displays all four detection methods across strategies. Random shows convergence estimates spanning 25-447, with Kneedle (94±25) marking the steepest descent region. Stratified methods cluster more tightly (56-122), with Practical confirming convergence at 94±25. Orbital knees show substantial

scatter (33-5,957) with large error bands, particularly for Threshold (5,957 \pm 880), reflecting gradual monotonic improvement rather than sharp convergence.

Prediction Stability



Cross-validation variance quantifies prediction reliability. Random maintained $\sigma=224$ nT at $n=20$, decreasing to $\sigma=4$ nT by $n=750$. Stratified showed superior stability ($\sigma=15$ nT at convergence) due to enforced lat-lon balance. Orbital exhibited $\sigma=40,000$ nT at $n=33$ —individual CV folds produced RMS spanning 10,000-50,000 nT, indicating fundamental model unreliability. The 1,800 \times variance ratio between orbital and random at small n confirms that longitude-limited sampling produces chaotic, unstable predictions unsuitable for scientific interpretation.

Key Results:

- Convergence: Random/stratified at $n=94$ (full lat-lon); orbital at $n=4,598$ (full lat, 1.1° lon).
- Timeline: Random/stratified require extended data collection for longitude coverage; orbital provides results in 1.3 hours.
- Coverage imbalance: Orbital oversamples latitude 360 \times relative to longitude.
- Stability: Orbital variance 1,800 \times worse at small n .

Limitations

Model and Data Constraints

My dipole model incorporates six free parameters (three dipole moment components and three spatial position coordinates), enabling off-center dipole reconstruction. However, the model assumes time-invariant fields over the 24-hour Swarm observation window, neglecting ionospheric currents, magnetospheric dynamics, and secular variation that introduce time-dependent external fields. Earth's magnetic field includes substantial crustal anomalies (up to 1,500 nT at satellite altitude) and higher-order multipole components that my dipole approximation cannot capture. The residual RMS errors of ~3,200 nT at convergence likely reflect these unmodeled field components rather than pure measurement noise. For planetary bodies with weaker dipole dominance (e.g., Mars crustal fields ~200 nT, Mercury's offset dipole), my findings may not translate directly since signal-to-noise characteristics and multipole importance differ fundamentally from Earth's configuration.

I analyzed a single 24-hour Swarm dataset at 460 km altitude with ~86,400 measurements at 1 Hz sampling. This altitude provides strong field measurements (peak magnitudes ~65,000 nT) with favorable signal-to-noise ratios, but sample efficiency may degrade at higher altitudes where field strength decreases as r^{-3} and measurement uncertainty becomes proportionally larger. The 24-hour window spans 15.4 orbits with 20° longitude precession, providing reasonable global coverage for

random/stratified sampling but potentially introducing geographic bias if used as representative of all possible orbital configurations. Different orbital inclinations, altitudes, or mission durations would alter the absolute sample requirements, though relative efficiency differences between strategies should remain qualitatively consistent.

Sampling Strategy Idealization

My "random sampling" strategy assumes measurements can be selected from arbitrary global locations after the full 24-hour dataset is collected. This is operationally unrealistic for real-time mission planning where measurements must follow orbital mechanics constraints. The approach represents post-mission data analysis or multi-satellite constellation scenarios where temporally/spatially distributed measurements can be retrospectively combined, but does not reflect single-spacecraft operational constraints during active data collection. Similarly, stratified sampling assumes perfect latitude-longitude grid binning, which requires either fortuitous orbital coverage or active mission planning to ensure balanced spatial distribution—potentially incompatible with other mission objectives (e.g., targeted regional studies, communication windows).

Orbital sampling uses strictly sequential chronological measurements, representing the most conservative real-time scenario where no spatial optimization is possible. However, even within orbital constraints, modest improvements could be achieved through adaptive downsampling (e.g., recording measurements only at specific latitude bands or longitude intervals) that I did not explore. My results therefore represent boundary cases: random/stratified provide optimal efficiency limits assuming complete spatial freedom, while orbital provides worst-case efficiency under maximum operational constraint.

Orbital Configuration Limitations

My analysis is restricted to Swarm's polar orbit configuration (87° inclination), which determines the fundamental spatial sampling geometry. Polar orbits naturally provide complete latitude coverage (-90° to $+90^\circ$) but sequential longitude coverage limited by orbital precession rate. This geometry explains why orbital sampling requires $49\times$ more data than globally distributed approaches—the latitude dimension is oversampled while longitude remains undersampled.

Different orbital inclinations would produce qualitatively different sampling patterns:

1. Equatorial orbits ($0\text{-}30^\circ$ inclination): Would reverse the problem—excellent longitude coverage but limited latitude range. For Earth's dipole field where pole-to-equator field strength varies 2:1, this could require even more samples than polar orbits to constrain dipole tilt.
2. Mid-inclination orbits ($30\text{-}60^\circ$): Would provide more balanced initial lat-lon sampling, potentially reducing the orbital vs. random efficiency gap below the $49\times$ ratio observed here.
3. Highly elliptical orbits: Would introduce altitude variation (field strength $\propto r^{-3}$), adding complexity not addressed by my almost constant-altitude analysis.

The sample size requirements and relative strategy efficiencies quantified in this work are specific to polar orbit geometry. Extrapolating these findings to other mission architectures requires orbital-mechanics modeling of spatial sampling patterns for each specific configuration.

Statistical and Computational Considerations

Monte Carlo cross-validation with 5-fold splitting and 50 independent runs provides robust uncertainty quantification, but the 250 total model fits per sample size may still underestimate tail risk for rare worst-case sampling configurations. My logarithmically-spaced sample sizes ($n=20, 94, 205, \dots, 10,000$) enable broad convergence characterization but may miss fine-scale structure in knee point transitions,

particularly for orbital sampling where convergence occurs gradually without sharp inflection. I employed least-squares optimization with Levenberg-Marquardt algorithm, which is sensitive to outliers and assumes Gaussian measurement noise. Robust fitting methods (e.g., iteratively reweighted least squares, RANSAC) might alter absolute sample requirements, particularly for orbital sampling at small n where extreme outliers occur frequently. My convergence criteria (RMS error, R^2 , MAE) emphasize prediction accuracy over physical parameter accuracy—dipole moment magnitude and position might converge at different rates than field prediction error, which I did not separately analyze.

Knee Detection Method Limitations

The four knee detection algorithms I implemented produce inconsistent results for orbital sampling, revealing fundamental limitations in convergence threshold identification. The threshold method (0.5% improvement criterion) identifies knees at **n=25 for random** but **n=5,957 for orbital**—a **~240x difference** suggesting the fixed percentage threshold is inappropriate for strategies with fundamentally different convergence rates. The curvature method locates maximum second derivatives in log-log space, but for orbital sampling's gradual monotonic improvement, multiple local maxima produce ambiguous results (n=2,338) that do not correspond to practical convergence.

The Kneedle algorithm detects orbital knee at n=77, far below the point where RMS error stabilizes (n~4,598), indicating the normalized curve-diagonal distance metric is oversensitive to early-stage fluctuations in noisy convergence profiles. The practical method (95% improvement threshold) gives n=35,493 for orbital-well beyond the point where random/stratified have fully converged—suggesting the baseline reference (worst-case performance) may be inappropriate for comparing across strategies with vastly different initial errors.

These discrepancies reflect a deeper problem: knee detection assumes a clear elbow-shaped curve with rapid transition from high-slope to low-slope regions. Random and stratified sampling exhibit this behavior (all four methods agree within factor of 2-3), but orbital sampling shows gradual logarithmic decay without sharp transition, violating the geometric assumptions underlying knee detection algorithms. For such profiles, "optimal" sample size depends entirely on chosen cost function (data collection cost vs. residual error) rather than intrinsic mathematical features of the convergence curve. I did not develop orbital-specific convergence criteria that account for this qualitative difference in error evolution.

Generalization to Planetary Missions

Earth's rapid rotation (24-hour period), strong dipole dominance (>90% of surface field), and near-axial alignment represent a specific field geometry that may not generalize to other bodies. Mercury's highly offset dipole (0.2 R_M northward displacement), Mars' extinct dynamo with dominant crustal sources, and ice moons' potential subsurface ocean induction require different model parameterizations where my dipole-focused findings may not apply directly. The relative importance of latitude vs. longitude sampling depends on dipole tilt and offset—my conclusion that latitude diversity dominates for Earth's near-aligned geometry would not hold for Mercury's 97° tilt or strongly offset configurations where longitude becomes critical for parameter disambiguation.

Mission timescale trade-offs depend on orbital parameters. Random and stratified sampling require sufficient orbital precession for global longitude coverage, with the minimum duration depending on orbit characteristics (e.g., Swarm's sun-synchronous 93.6-minute orbit with 1.3°/orbit precession would require multiple days to weeks for adequate coverage). Determining precise requirements for different mission architectures requires analysis beyond this 24-hour study. Different mission architectures (e.g., highly elliptical orbits, polar vs. equatorial inclinations, multiple satellites) would fundamentally alter the

data collection timeline and spatial coverage patterns. My results provide scaling insights for Swarm-like configurations but require recalculation for specific mission geometries.

Discussion

Physical Interpretation: Why Spatial Balance Matters

The $49\times$ efficiency gap between random and orbital sampling strategies reflects fundamental information geometry constraints in inverse problems. Dipole parameter estimation requires measurements that constrain all six model parameters (three moment components, three position coordinates) with balanced sensitivity. Random and stratified sampling achieve this through isotropic spatial coverage, producing well-conditioned jacobian matrices. Orbital sampling concentrates measurements along meridional tracks, creating anisotropy where latitudinal gradients are oversampled $360\times$ relative to longitudinal variations.

This imbalance manifests mathematically as ill-conditioning: the jacobian matrix has eigenvalues spanning multiple orders of magnitude, rendering solutions sensitive to measurement noise. The $1800\times$ variation amplification I observed at small n directly reflects this ill-conditioning—small perturbations in the training set produce different parameter estimates because longitudinal components remain nearly unconstrained. Convergence occurs only when sufficient meridional tracks accumulate ($n\sim 4,598$, covering 1.1° longitude) to constrain longitudinal dipole structure through latitudinal sampling along multiple nearby tracks.

The latitude-longitude asymmetry has physical origins in dipole field geometry. For Earth's near-axially aligned field, pole-to-equator field strength varies by a factor of 2, while azimuthal variations at fixed latitude are minimal. Latitudinal diversity therefore provides stronger parameter constraints than longitudinal diversity for near-aligned configurations. However, my six-parameter model includes off-center positioning (x_0 , y_0 , z_0), which introduces azimuthal asymmetries requiring longitude sampling for disambiguation.

Comparison with Planetary Mission Data

My results provide context for interpreting existing planetary magnetic field missions. The Mars Global Surveyor (MGS) mission operated in a sun-synchronous polar orbit, accumulating measurements with spatial clustering along repeating ground tracks (Acuña et al., 1999). The MESSENGER mission at Mercury collected magnetometer measurements over 4 years (Anderson et al., 2012), with orbital precession providing better longitude coverage than single-day datasets. Random and stratified sampling require extended mission duration for adequate spatial coverage, suggesting that Mercury's offset dipole likely required extended mission phases for robust parameter constraints.

For the Swarm mission specifically, my findings indicate that dipole moment estimation from the full three-satellite constellation benefits from the naturally distributed spatial sampling across different orbital phases (European Space Agency, 2013). Multi-satellite architectures partially mitigate the single-orbit clustering problem by providing simultaneous measurements at different longitudes.

Knee Detection and Convergence Assessment

The inconsistency of knee detection algorithms for orbital sampling reveals that convergence metrics developed for smooth optimization problems may not transfer directly to spatially-constrained inverse problems. The spread in knee estimates for orbital sampling ($n=33$ to 5,957 across four methods, with uncertainties up to ± 930) indicates that orbital convergence is gradual and asymptotic rather than exhibiting clear inflection points.

This has practical implications for mission operations. Early-mission dipole estimates using orbital data

require explicit uncertainty quantification through methods like Monte Carlo cross-validation rather than relying on convergence heuristics. The negative R^2 values I observed at small n for orbital sampling demonstrate that standard fit quality metrics can fail under spatial ill-conditioning. Mission planning should account for this by either designing orbits with explicit longitude precession targets or accepting that early-mission estimates require substantially more data with formal error quantification.

Methodological Contributions

The Monte Carlo cross-validation framework with 5-fold CV and 50 independent runs per configuration provides robust uncertainty quantification for inverse problems with spatial sampling constraints. The use of four orthogonal knee detection algorithms (threshold, curvature, Kneedle, practical) demonstrates that convergence assessment requires multiple metrics rather than single-criterion optimization. The variance analysis showing 1,800 \times amplification for poorly-conditioned sampling configurations quantifies the prediction instability that can arise from spatial clustering.

The framework I developed is generalizable to other planetary magnetometry applications where spatial sampling patterns are constrained by orbital mechanics. The key insight—that spatial distribution matters more than sample count—applies broadly to inverse problems in geophysics where observation locations are operationally constrained (Maurer et al., 2010).

Conclusion

This study quantified the efficiency penalty imposed by orbital sampling constraints on planetary magnetic dipole estimation through Monte Carlo cross-validation of three sampling strategies applied to Swarm magnetometer data. Random and stratified sampling achieved convergence at $n=94$ measurements ($RMS \sim 3,200$ nT, $R^2=0.976$). Orbital sampling converged at $n=4,598$, requiring 49 \times more measurements due to latitude-longitude sampling imbalance.

Four independent knee detection algorithms agreed on $n \sim 90$ -200 convergence for random/stratified strategies but produced inconsistent results for orbital ($n=77$ to 40,877), indicating gradual asymptotic improvement rather than clear optimal thresholds. Cross-validation variance analysis revealed 1,800 \times amplification in prediction uncertainty for orbital sampling at small sample sizes, reflecting jacobian matrix ill-conditioning from spatial clustering.

These findings establish that spatial distribution fundamentally determines inverse problem quality in satellite magnetometry. For the specific case of Swarm data at 460 km altitude, random/stratified approaches achieved target accuracy with 0.1% of available measurements when global spatial coverage was available, while orbital approaches required 5.3% of data due to meridional track concentration. The magnitude of this efficiency difference depends on field geometry, measurement noise characteristics, and mission orbital parameters.

The Monte Carlo validation framework developed here provides a template for assessing sampling requirements in mission planning contexts. Future work could extend this analysis to higher-order multipole models, different orbital configurations, and multi-satellite constellation architectures to provide mission-specific guidance for planetary magnetometry campaigns.

For mission planning, these results suggest two operational regimes: (1) rapid preliminary estimates can be obtained from sequential orbital data within hours, accepting 49 \times data overhead, or (2) high-efficiency estimates require mission architectures that ensure longitude diversity through multi-satellite constellations, orbital precession, or extended mission durations. The choice depends on mission constraints and scientific objectives.

References

- Acuña, M. H., Connerney, J. E. P., Ness, N. F., Singer, R. B., Linker, J. A., & Wasilewski, P. (1999). Global distribution of crustal magnetization discovered by the Mars Global Surveyor. *Science*, 284(5415), 790–793.
- Anderson, B. J., Johnson, C. L., Korth, H., Purucker, M. E., Winslow, R. M., Slavin, J. A., ... & McNutt, R. L. (2012). The structure of Mercury's magnetic field from MESSENGER's magnetometer. *Geophysical Research Letters*, 39, L04201.
- Aubert, J. (2018). Geomagnetic forecasts driven by thermal wind dynamics in the Earth's core. *Geophysical Journal International*, 203(3), 1738–1751.
- Baumjohann, W., & Treumann, R. A. (1996). *Basic space plasma physics*. World Scientific Publishing.
- Christensen, U., & Aubert, J. (2006). Scaling properties of convection-driven dynamos in rotating spherical shells and application to planetary magnetic fields. *Geophysical Journal International*, 166(1), 97–114.
- Connerney, J. E. P., Kotsiaros, S., Oliiversen, R. J., Espley, J. R., Joergensen, J. L., Joergensen, P. S., ... & Bolton, S. J. (2018). The Juno magnetic field investigation. *Space Science Reviews*, 213(2), 39.
- European Space Agency. (2013). *Swarm: Earth's magnetic field and environment explorers*. ESA Communications.
- Finlay, C. C., Lesur, V., Beggan, C. D., Chulliat, A., Lowes, F. J., Macmillan, S., & Olsen, N. (2016). International Geomagnetic Reference Field: The 12th generation. *Geophysical Journal International*, 206(2), 1112–1121.
- Jakosky, B. M., & Edwards, C. S. (2018). Inventory and implications of CO₂ detected by MAVEN. *Nature Astronomy*, 2(2), 145–150.
- Jones, C. A. (2011). Planetary magnetic fields and fluid dynamos. *Annual Review of Fluid Mechanics*, 43, 583–614.
- Langlais, B., Thébault, E., Houliez, A., Purucker, M. E., & Lillis, R. J. (2019). A new model of the crustal magnetic field of Mars using MGS and MAVEN. *Journal of Geophysical Research: Planets*, 124(6), 1542–1569.
- Levenberg, K. (1944). A method for the solution of certain non-linear problems in least squares. *Quarterly of Applied Mathematics*, 2(2), 164–168.
- Marquardt, D. W. (1963). An algorithm for least-squares estimation of nonlinear parameters. *Journal of the Society for Industrial and Applied Mathematics*, 11(2), 431–441.
- Maurer, H., Curtis, A., & Boerner, D. E. (2010). Recent advances in optimized geophysical survey design. *Geophysics*, 75(5), 75A177–75A194.
- Menke, W. (2012). *Geophysical data analysis: Discrete inverse theory* (3rd ed.). Academic Press.
- Metropolis, N., & Ulam, S. (1949). The Monte Carlo method. *Journal of the American Statistical Association*, 44(247), 335–341.
- Olsen, N., Lühr, H., Finlay, C. C., Sabaka, T. J., Wandres, M., Kotsialos, S., & Coxon, J. (2016). The CHAOS-6 geomagnetic field model. *Geophysical Journal International*, 212(1), 331–356.
- O'Rourke, J. G., Connerney, J. E. P., Stevenson, D. J., Langlais, B., & Weiss, B. P. (2019). Detectability of remanent magnetism in the crust of Venus. *Geophysical Research Letters*, 46(9), 4735–4741.
- Satopää, V., Albrecht, J., Irwin, D., & Raghavan, B. (2011). Finding a "kneedle" in a haystack: Detecting knee points in system behavior. *2011 31st International Conference on Distributed Computing Systems Workshops*, 166–171.
- Soderlund, K. M., Heimpel, M. H., King, E. M., & Aurnou, J. M. (2020). The underexplored frontier of ice giant dynamos. *Journal of Geophysical Research: Planets*, 125(11), e2020JE006418.
- Virtanen, P., Gommers, R., Oliphant, T. E., Haberland, M., Reddy, T., Cournapeau, D., Burovski, E., Peterson, P., Weckesser, W., Bright, J., van der Walt, S. J., Brett, M., Wilson, J., Millman, K. J.,

- Mayorov, N., Nelson, A. R. J., Jones, E., Kern, R., Larson, E., ... SciPy 1.0 Contributors. (2020). SciPy 1.0: Fundamental algorithms for scientific computing in Python. *Nature Methods*, 17(3), 261–272.
- Aster, R. C., Borchers, B., & Thurber, C. H. (2019). *Parameter Estimation and Inverse Problems* (3rd ed.). Elsevier.
- Menke, W. (2018). *Geophysical Data Analysis: Discrete Inverse Theory* (4th ed.). Academic Press.
- Tarantola, A. (2005). *Inverse Problem Theory and Methods for Model Parameter Estimation*. SIAM.

Acknowledgments

The theoretical framework for dynamo action and magnetic field generation is based on course materials.

Perplexity AI assisted with grammar correction and writing consistency. Claude AI assisted with code review and error identification in the Python implementation.

All code, data, and supplementary figures used in this study are publicly available at:

GitHub Repository: [Project](#)